Hydrophobic nanoscale ribs alter the condensation mode of water vapor: A molecular dynamics simulation

Le Chen（陈乐）[a], Ze-long Luo（骆泽龙）[a], Lian-xiang Ma（马连湘）[a], Yuan-zheng Tang（唐元政）[a,*]

[a]*College of Electromechanical Engineering, Qingdao University of Science and Technology, Qingdao, 266061, China*

Corresponding author: Yuan-zheng Tang

E-mail: tangyuanzheng@qust.edu.cn

Abstract

This study employs molecular dynamics simulations to investigate the condensation behavior of water vapor on nano-ribbed copper substrates featuring three distinct rib heights and tunable surface wettability, with the primary objective of elucidating the microscopic mechanisms governing the critical potential well depth at which the transition from dropletwise to filmwise condensation occurs as a function of increasing nanoscale ribs height. By modulating the surface wettability via systematic variation of the potential well depth between copper and oxygen atoms, the study constructed three sets of nanorib models—low-rib (LC, 10 Å), medium-rib (MC, 20 Å), and high-rib (HC, 30 Å)—and conducted quantitative analyses of condensation morphology, intrinsic contact angles, and the evolution of the system's potential energy. The results demonstrate that the wettability of the nanoscale rib is the key factor governing the condensation morphology: hydrophobic nanoscale ribs can transform a flat substrate—which would otherwise exhibit filmwise condensation—into dropwise condensation, whereas hydrophilic nanoscale ribs sustain continuous liquid film growth. Moderate increases in nanoscale ribs height can reduce the dependence of condensation morphology on wettability while simultaneously elevating the critical potential well depth required for the condensation mode transition. On low-rib (LC) substrates, an abrupt morphological transition occurs at a potential well depth of 0.007 eV, with a complete shift to filmwise condensation at 0.010 eV. On medium-rib (MC) substrates, a continuous liquid film forms only when the potential well depth reaches 0.011 eV. For high-rib (HC) substrates, the critical potential well depth for the condensation transition is 0.008 eV. When the characteristic height of the nanoscale rib in the Z-direction is comparable to the thickness of the condensed water layer, the modulating effect of wettability on the condensation contact angle is most pronounced. This study elucidates the synergistic regulatory mechanism by which nanostructure height and surface wettability govern the phase transition of water vapor, thereby offering a novel theoretical foundation for the structural optimization of atmospheric water-harvesting substrates.

Keywords: Atmospheric water harvesting; Wettability; Condensation mode; Molecular dynamics simulation.

PACS: 92.60. J-, 68.08. Bc, 68.03. Fg, 02.70. Ns

1. Introduction

In recent years, the escalating shortage of freshwater resources has motivated a growing number of researchers to focus on advancing water collection technologies. Current water collection techniques encompass seawater desalination [1], wastewater treatment [2], and atmospheric water harvesting [3]. Active collection methods, such as desalination and wastewater treatment, are resource-intensive, economically costly, and contribute to greenhouse gas emissions, including carbon dioxide. In contrast, passive water collection—which extracts water directly from the Earth's atmosphere—is low-cost and pollution-free, and has emerged as a promising solution to alleviate water scarcity [4–6]. Water vapor undergoes heterogeneous nucleation on solid surfaces and subsequently detaches, thereby completing the atmospheric water-harvesting cycle. Different structural surfaces and wettabilities influence the condensation patterns and effectiveness of this process [7–9]. For instance, the surface of a lotus leaf is covered with nanoscale waxy crystals that form a hierarchical nanostructure, reducing the water-solid contact area and thereby imparting superhydrophobic properties. Consequently, water vapor condenses on its surface in a dropwise manner. The African Stenocara gracilipes beetle possesses a microstructured back that alternates between hydrophilic and hydrophobic regions. The hydrophilic raised areas, characterized by higher surface energy, preferentially adsorb water molecules, whereas the hydrophobic regions, with lower surface energy, resist droplet adhesion, thereby promoting condensation and facilitating droplet removal [10]. This biomimetic strategy has inspired extensive research on hybrid-wettability and textured surfaces for enhanced condensation performance [11–14]. Jin et al. [15] experimentally demonstrated that discontinuous strip substrates can increase water collection efficiency by 40% and proposed a novel structural design. Gao et al. [16] fabricated beetle-inspired mixed-wettability fabrics and validated their superior vapor capture performance in large-scale harvesting tests.

Although the aforementioned experimental studies confirm that substrate nanostructures and heterogeneous wettability dominate condensation performance, experimental techniques alone cannot capture the transient molecular-scale evolution of condensation clusters, droplet coalescence, or the details of interfacial interactions. Molecular dynamics (MD) simulation overcomes this limitation by tracking atomic trajectories and elucidating microscopic phase-transition mechanisms, and has thus been widely adopted to investigate nanoscale vapor condensation behavior.

Chinese researchers have conducted targeted MD simulations on copper-based condensation substrates. Gong et al. [17] established two-stage microgroove models, quantified the coupled influence of multi-dimensional structural parameters on vapor condensation, and identified the optimal hierarchical groove configuration for enhanced condensate harvesting capacity. Xing et al. [18] employed argon as a representative non-condensable gas to investigate its interference with flow and heat transfer within nanochannels, revealing that low-concentration argon enhances interfacial slip, whereas excessive gas impedes mass transport—an effect that can be mitigated by elevated temperatures. Nurrohman et al. [19] compared condensation

performance under varying graphene coverage on copper surfaces and concluded that thin, discontinuous graphene coatings are more conducive to vapor nucleation and interfacial heat transfer.

International researchers have constructed various multi-scale simulation models to elucidate the microscopic condensation mechanisms at the nanoscale. Teodori et al. [20] developed a cross-scale coupling model and introduced a Tolman-length correction to address the calculation deviation of classical nucleation theory, systematically demonstrating how contact angle governs the transition between dropwise and filmwise condensation. Kim et al. [21] combined simulation and experimental approaches to characterize capillary condensation within amphiphilic nanopores, quantifying how pore wettability and particle size modulate vapor capture efficiency. Mehereen et al. [22] performed MD simulations on platinum surfaces with sinusoidal gradient wettability, verifying that multi-order sinusoidal structures significantly enrich nucleation sites while simultaneously enhancing condensation mass flux and heat exchange efficiency. Yang et al. [23] investigated the laminar transport behavior of shear-thinning fluids in microchannels via molecular dynamics simulations, revealing the microscopic origin of shear thinning through analyses of velocity distribution, intermolecular energy, and hydrogen-bond evolution. Liu et al. [24] performed molecular dynamics simulations to reveal the evolution of irradiation-induced defects in nanocrystalline tungsten with varying grain sizes under different primary knock-on atom (PKA) energies and incident directions. Wang et al. [25] employed molecular dynamics simulations in conjunction with generalized stacking fault energy (GSFE) analysis and a modified Peierls–Nabarro model to elucidate the competitive slip and twinning deformation mechanisms in γ-phase U–Mo alloys as a function of Mo concentration.

Shi et al. [26] focused on vapor nucleation preference on single wavy copper surfaces, analyzing only the influence of concave cavity size on nucleation potential energy without considering the coupled effects of structural height and wettability on the condensation transition. Wei et al. [27] limited their discussion to uniform-wettability flat surfaces under variable vapor concentrations, neglecting heterogeneous patterned nanostructures. Wang et al. [28] analyzed planar substrates decorated with isolated hydrophilic dots but did not incorporate three-dimensional vertical rib structures, and thus failed to clarify how rib height delays the transition between dropwise and filmwise condensation.

Existing MD studies have predominantly analyzed the effects of surface topography or wettability on water vapor condensation in isolation; very few have quantitatively investigated how the height of vertical nanoscale ribs and continuously tunable wettability jointly regulate the critical threshold for condensation mode transitions. Most existing nanostructured models employ a single fixed rib height and lack comparative analyses across low-, medium-, and high-rib groups with respect to the critical potential well depth for the droplet-to-film condensation transition. Furthermore, comprehensive explanations for the abrupt changes in contact angle and the accompanying evolution of system potential energy remain scarce.

To address these research gaps, the present study constructed three sets of copper substrates with vertically oriented hydrophobic nanoscale ribs—low-rib (LC: 10 Å), medium-rib (MC: 20 Å), and high-rib (HC: 30 Å)—and continuously varied the potential well depth of the copper–oxygen atomic interaction (0.002–0.012 eV) to achieve comprehensive control over wettability across the full range. Using MD simulations, we systematically analyzed transient condensation morphologies, changes in intrinsic contact angles, and the evolution of the system's potential energy to elucidate the core mechanism by which moderately increasing the height of the nanoribs delays the critical potential well at which condensation transitions from droplet to film formation, and quantitatively compared the thresholds for this transition across the three rib structures. This study refines the microscopic theory of the synergistic regulation of water vapor condensation by nanostructures and wettability, providing new insights for the structural optimization of high-efficiency atmospheric water-harvesting substrates.

2.Simulation and method

As shown in Fig. 1, the simulation system consists of two copper (Cu) plates, hydrophobic nanoscale ribs, and water molecules placed in the intervening space. Each Cu plate comprises 12 layers of (100)-oriented Cu atoms, with a cross-sectional area of 100.29 Å × 100.29 Å. The central vapor region measures 100.29 Å × 100.29 Å × 610 Å. The vapor density is set to the saturation vapor density at 600 K, with a total of 9748 water molecules. Periodic boundary conditions are applied in all three Cartesian directions.

The lower Cu plate is divided into functional layers: the bottom two atomic layers are fixed to prevent model displacement that could compromise simulation accuracy; the middle six layers constitute a constant-temperature layer that regulates the temperature of the lower Cu plate; and the upper four layers are free layers governed by the microcanonical (NVE) ensemble, ensuring that atomic motion follows Newton's second law and accurately captures the interfacial interactions between the Cu surface and water molecules. The top two layers of the upper Cu plate are fixed, while the remaining layers serve as constant-temperature layers. Additionally, the nanoscale ribs are configured at three distinct heights—low (LC, 10 Å), medium (MC, 20 Å), and high (HC, 30 Å)—with a uniform width of 10 Å spanning the entire plane. This design is intended to investigate the effects of nanoscale rib height on water vapor condensation behavior and to analyze its influence on the condensation mode transition, thereby providing theoretical support and benchmark data for the optimization of water collection systems.

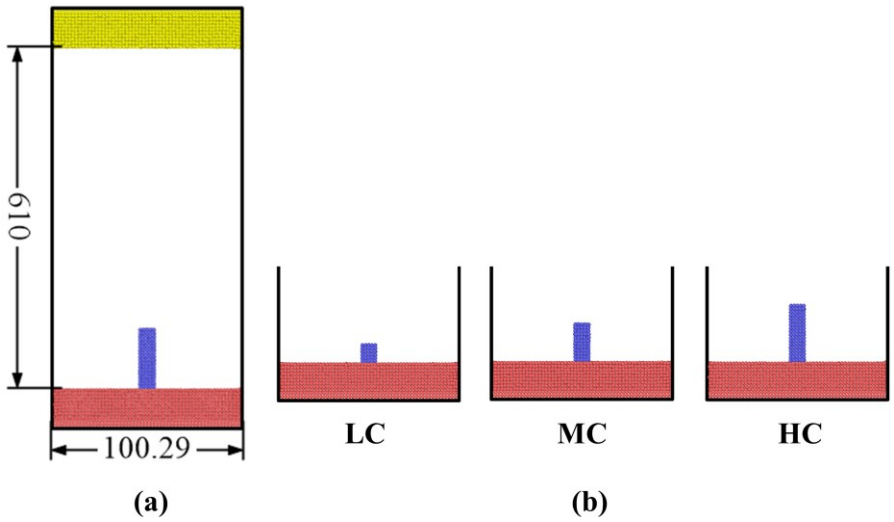


Fig. 1: (a) Simulation model; (b) LC: The height of the nanoscale rib is 10 Å; MC: The height of the nanoscale rib is 20 Å; HC: The height of the nanoscale rib is 30 Å.

The embedded atomic potential function (EAM) is used to describe the interaction between Cu-Cu [29],

$$E_s = F_\alpha\left(\sum_{i\neq j}\rho_\beta(r_{ij})\right)+\frac{1}{2}\sum_{i\neq j}\phi_{\alpha\beta}(r_{ij}) \tag{1}$$

Where F is the embedding energy as a function of the atomic electron density ρ, the φ is a pair potential interaction, a and β are the element type of atom i and atom j.

The water model adopts SPC/E model [30]，The 12-6 Lennard-Jones（L-J）and Coulombic potentials with a cutoff distance of 10 Å describe the atomic interactions between water and water, as well as between water and substrate [31]:

$$U_{ij} = 4\varepsilon_{ij}\left[\left(\frac{\sigma_{ij}}{r_{ij}}\right)^{12}-\left(\frac{\sigma_{ij}}{r_{ij}}\right)^{6}\right]+\frac{1}{4\pi\varepsilon_0}\frac{q_i q_j}{r_{ij}} \tag{2}$$

Where ε represents the depth of potential well, and σ represents the distance when the inter-particle potential is zero. r_{ij} represents the distance between atom i and atom j. q_i and q_j represent the electric charges of between atom i and atom j. ε_o is the permittivity of the vacuum.

In this study, the parameter $\sigma_{Cu\text{-}O}$ is set to 3.190 Å [32].This study focuses on the copper-oxygen potential well depth range of 0.002–0.012 eV, which fully covers the range from strongly hydrophobic to moderately hydrophilic wetting conditions. This range allows for the comprehensive capture of the critical values for the nanorib-to-film condensation transition across low, medium, and high rib height groups, enabling a quantitative comparison of the transition potential wells at different rib heights. For hydrophilic surfaces, $\varepsilon_{Cu\text{-}O}$ is set to 0.017 eV, while for the nanoscale ribs parameters, $\varepsilon_{Cu\text{-}O}$ is set to range from 0.002 eV to 0.012 eV to investigate the effect of the wettability of the nanoscale ribs on vapor condensation. The particle–particle particle–mesh (PPPM) method is adopted to compute long-range Coulombic forces. The atomic structure of the Cu plate is identical to that of the

hydrophobic nanoscale ribs, with the sole difference being the energy parameters of the interaction forces. To prevent inaccuracies arising from variations in water molecule bond lengths and angles during the simulation, the SHAKE algorithm is employed to constrain these degrees of freedom [33]. The SHAKE constraint algorithm enforces fixed O–H bond lengths and H–O–H bond angles for each SPC/E water molecule after every integration step. This eliminates non-physical deformations induced by molecular thermal motion, stabilizes the system potential energy, and ensures that condensation morphologies and contact angle data are comparable across all operating conditions.

The simulation system is first subjected to energy minimization and subsequently equilibrated at 600 K using the Langevin thermostat for 5 ns. During this equilibration phase, H_2O molecules evaporate within the model; upon reaching thermal equilibrium, the internal vapor reaches saturation pressure. During the condensation stage, the constant-temperature layer of the lower Cu plate is maintained at 298 K, while the upper Cu plate is held at 600 K to prevent energy loss from water molecules contacting the upper plate, which could otherwise compromise the accuracy of the simulation results. The simulation time step is set to 1 fs, and the total condensation duration is 2 ns. All simulations are performed using the LAMMPS package [34], and the resulting trajectories are visualized and analyzed using OVITO [35].

In this study, the condensation simulation duration is uniformly fixed at 2 ns for all wettability conditions. Hydrophobic substrates require the full 2 ns to form a stable water column, while moderately wettable substrates necessitate the complete time-series data to capture the critical point of contact-angle transition. Although fully hydrophilic substrates reach a stable filmwise condensation state within 1.4 ns, standardizing the simulation duration eliminates time-variable interference and ensures fairness in the quantitative comparison of transition thresholds across all groups.

3.Result

3.1 The effect of Hydrophobic nanoscale ribs

According to classical nucleation theory, hydrophobic sites and surface roughness features can elevate the local nucleation barrier. An increase in this barrier alters the condensation behavior of water vapor and ultimately influences the resulting condensation morphology. Upon introducing hydrophobic nanoscale ribs onto a hydrophilic flat substrate, a marked change in the water vapor condensation morphology is observed. As shown in Fig. 2 (where green atoms denote hydrogen, purple atoms denote oxygen, red atoms denote Cu, and blue atoms denote Cu with modified wettability), water vapor condenses in a filmwise manner on the flat surface, whereas on the substrate with hydrophobic nanoscale ribs, the condensation mode transitions from filmwise to dropwise.

We postulate that this transition arises from the hydrophobicity of the nanoscale ribs, which compels vapor to nucleate preferentially on both sides of each rib. Owing to the strong hydrophobicity, water molecules on either side face a high energy barrier

to traversing the central rib, thereby inducing a change in the overall condensation morphology. To discern whether the altered condensation mode is attributable to the rough morphology of the nanoribbed surface or to the hydrophobicity of the ribs themselves, we adjusted the wettability of the nanoscale ribs to match that of the flat surface—i.e., rendering them hydrophilic—and compared the results. In Fig. 3(b), where the nanoscale ribs are hydrophilic, the final condensation mode is filmwise. In contrast, in Fig. 3(a), where the nanoscale ribs are hydrophobic, the condensation mode is dropwise.

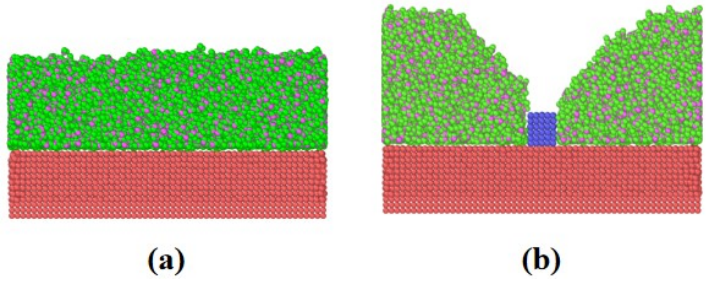


Fig.2: Water vapor condensation on plane substrate surfaces and surfaces with hydrophobic nanoscale rib: (a) Plane surface; (b) LC.

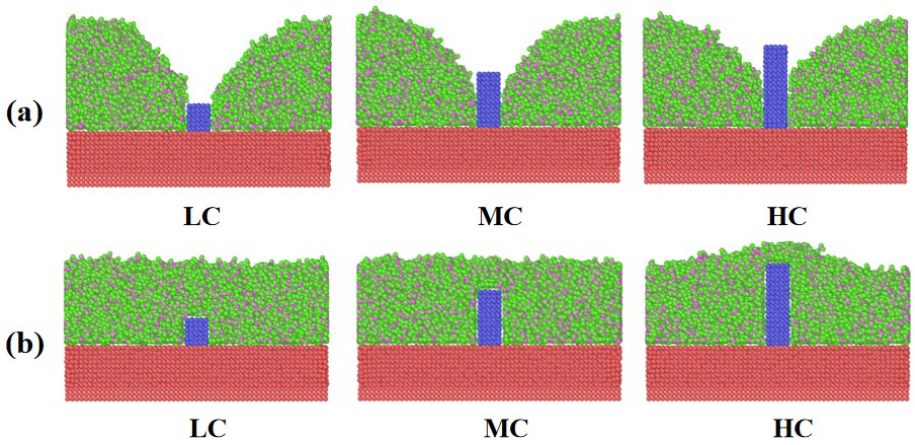


Fig.3 Water vapor condensation on the surface of nanoscale ribs with different heights and wettability**:** (a) hydrophobic nanoscale rib; (b) Hydrophilic nanoscale rib.

To further explore the influence of rib wettability on the condensation process, we selected the LC model as a representative case for comparing condensation on hydrophobic versus hydrophilic nanoscale ribs. As shown in Fig. 4, water vapor initially condenses on both sides of the hydrophobic nanoscale ribs, with a distinct dropwise morphology emerging at 0.21 ns. This morphology persists and grows throughout the condensation process, ultimately forming discrete water columns. In contrast, when water vapor condenses on hydrophilic nanoscale ribs, condensation occurs not only on the sides of the ribs but also directly on their surfaces, growing in the form of a continuous liquid film. As condensation proceeds, the film continues to expand until the end of the simulation. Therefore, the change in condensation mode is strongly correlated with the wettability of the nanoscale ribs. This influence will be examined in detail in the following section.

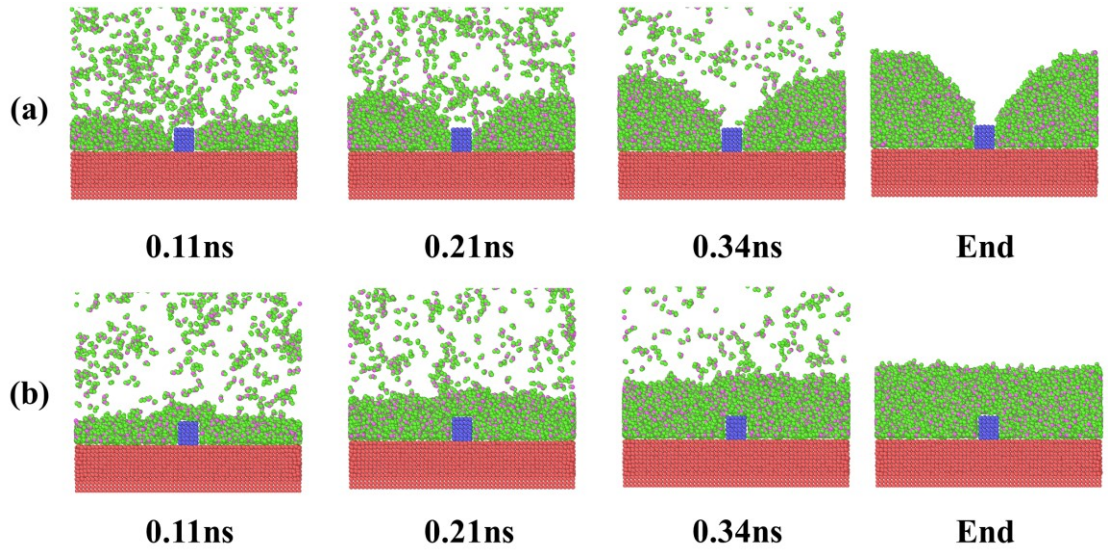


Fig.4 Condensation process of water vapor on hydrophilic and hydrophobic nanoscale rib at different times: (a) hydrophobic nanoscale rib; (b) Hydrophilic nanoscale rib.

3.2 The effect of wettabilities

To investigate the effect of nanorib wettability on water vapor condensation morphology, the potential well depth between oxygen and copper atoms was systematically adjusted to modulate the wettability of the Cu substrate surface. During the adjustment process, all other parameters remained unchanged. Figs. 5–7 present the condensation morphologies of water vapor on LC, MC, and HC nanoribbed substrates, respectively.

As shown in Fig. 5, the condensation morphology remains in the form of discrete water columns when the potential well depth is below 0.006 eV. However, a dramatic transition occurs beyond this threshold, with the morphology shifting from dropwise to filmwise. A similar phenomenon is observed in the HC case (Fig. 7), where the contact angle of the water column decreases with increasing potential well depth. At a depth of 0.008 eV, the condensation morphology transitions to a filmwise configuration. In contrast, for the MC case, even as the potential well depth increases to 0.010 eV, the condensation morphology does not transition to a liquid film; it remains in the form of water columns. This pronounced influence of nanoscale rib height on the condensation morphology transition further confirms that, at the nanoscale, condensation behavior is not governed by macroscopic surface geometry. At this scale, most surfaces appear smooth; however, when the substrate surface structure is commensurate with the condensation scale, the condensation behavior becomes sensitive to the surface morphology, in contrast to macroscopic observations [36].

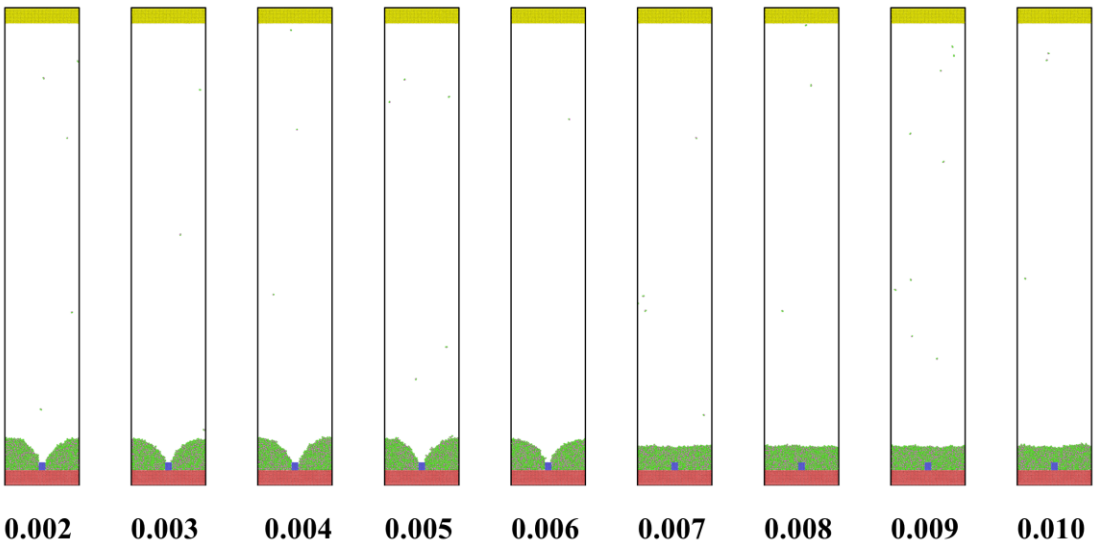


Fig.5: Condensation morphology of water vapor on LC substrate with different wettability nanoscale ribs.

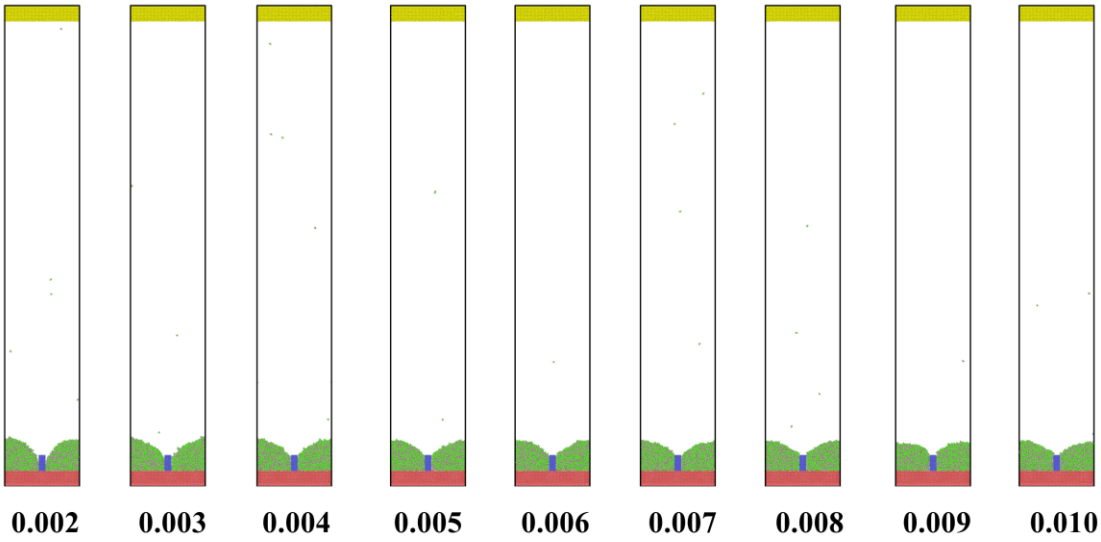


Fig.6: Condensation morphology of water vapor on MC substrate with different wettability nanoscale ribs.

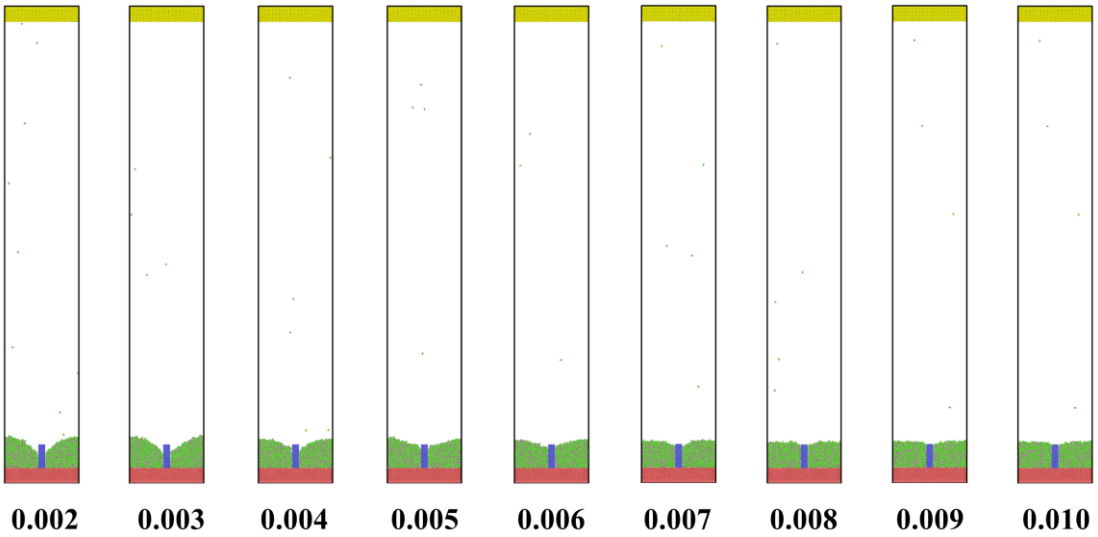


Fig.7: Condensation morphology of water vapor on HC substrate with different wettability nanoscale ribs.

To explore the interrelationship between nanorib height, wettability, and condensation morphology, the intrinsic contact angle of the condensed water was measured. Fig. 8 illustrates the measurement method, where θ denotes the contact angle at the condensation interface. To minimize measurement errors, the left and right contact angles were averaged, and three independent measurements were performed for each condition. The final measurements of the intrinsic contact angle as a function of wettability are shown in Fig. 9.

It is evident that for the LC group, the intrinsic contact angle remains relatively constant until the potential well depth reaches 0.006 eV. At 0.007 eV, however, an abrupt transition occurs, with the contact angle dropping to 90°. For the MC group, the intrinsic contact angle decreases progressively with increasing potential well depth. This decrease is attributed to the enhanced water–nanoscale rib interaction, which promotes the migration of water molecules from both sides of the ribs toward the substrate plane between adjacent ribs, thereby reducing the intrinsic contact angle. For the HC group, the intrinsic contact angle decreases gradually with increasing potential well depth, until at 0.008 eV, where it undergoes an abrupt transition to 90°. This abrupt change in the intrinsic contact angle prompts the question of whether it arises from a change in the condensation mode or is merely a consequence of the wettability variation. This understanding is crucial for elucidating the mechanisms of water vapor condensation, which we will discuss in detail in the next section.

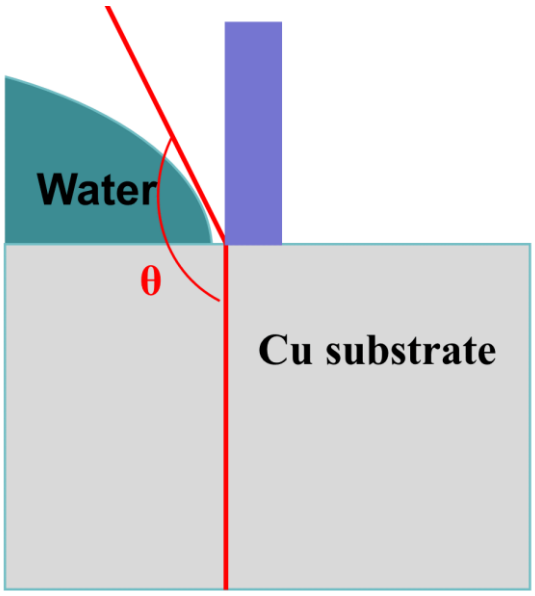


Fig.8: Intrinsic contact angle measurement schematic.

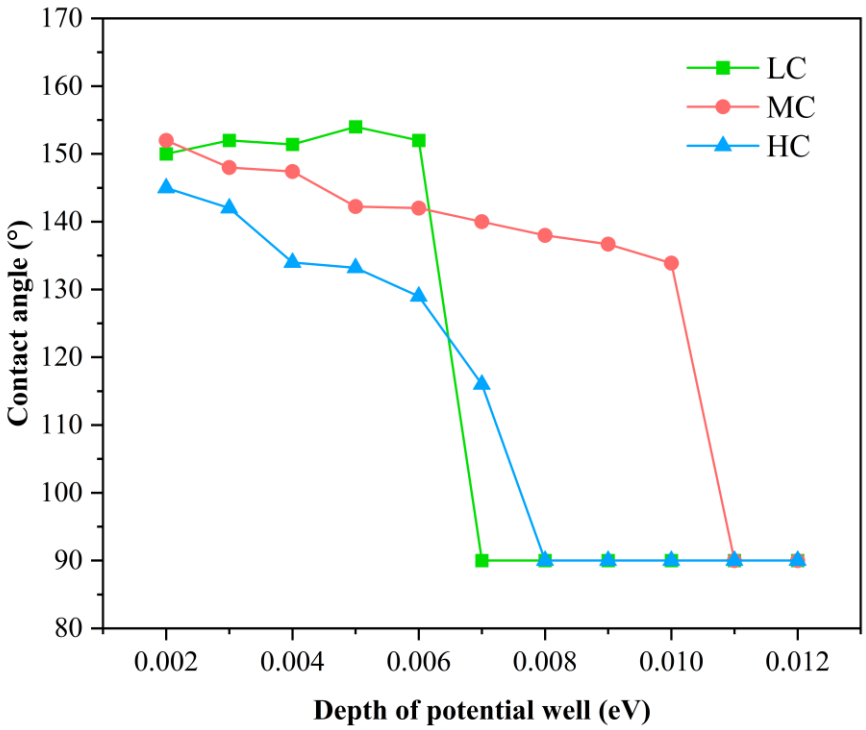


Fig.9: Water vapor condenses at different contact angles on the surface of nanoscale ribs substrates with varying wettability and height.

3.3 Reasons for intrinsic contact angle mutation

During water vapor condensation, the release of latent heat lowers the system potential energy, and the rate of this decrease is related to the condensation mode and the final morphology. Therefore, we statistically analyzed and computed the potential energy changes over time during the condensation process, as shown in Fig. 10.

The sawtooth-shaped capillary grooves formed between adjacent nanoribs generate microscale capillary forces. Under hydrophobic conditions, capillary

confinement restricts lateral liquid spreading and delays film formation. When interfacial adsorption is enhanced, capillary traction drives water droplets over the tops of the ribs, promoting coalescence across the grooves. Concurrently, the groove structure increases the nucleation surface area, provides low-potential-energy nucleation sites, and locally retains the latent heat of condensation. These factors collectively explain the mechanism by which taller nanoribs elevate the critical potential well for the condensation transition.

At the molecular scale, the abrupt change in contact angle and the accompanying sharp drop in system potential energy are jointly governed by variations in the copper–oxygen van der Waals interaction strength and the concomitant reorganization of the water hydrogen-bond network. Under low-potential-well (strongly hydrophobic) conditions, copper–oxygen adsorption is weak; water molecules aggregate into disconnected, isolated water columns, with hydrogen bonds forming only within individual clusters. There are virtually no bridging hydrogen bonds across the ribs, resulting in a relatively high system potential energy and a stable dropwise condensation morphology. When the potential well depth exceeds a critical value, the copper–oxygen attractive forces increase significantly, disrupting the isolated water clusters on either side of the rib and enabling the formation of continuous, interconnected hydrogen-bond networks within the rib gaps. The large number of newly formed hydrogen bonds rapidly releases the latent heat of the phase transition, causing a sharp drop in system potential energy, which manifests macroscopically as a transition from dropwise to filmwise condensation. Taller nanoribs exert a stronger capillary confinement effect on the water columns, requiring a larger critical potential well to enable the separated water clusters to interconnect. This provides a molecular-level explanation for the delayed critical potential well observed for the condensation transition in the medium- and high-rib structures.

It is evident that for potential well depths from 0.002 eV to 0.006 eV, the potential energy evolution curves exhibit significant overlap. However, at 0.007 eV, the rate of potential energy decrease accelerates, corresponding to the abrupt change in the final contact angle. To verify whether this abrupt change corresponds to a shift from dropwise to filmwise condensation, the instantaneous morphologies at the potential well depths where the potential energy exhibited sudden changes were analyzed, as shown in Fig. 11.

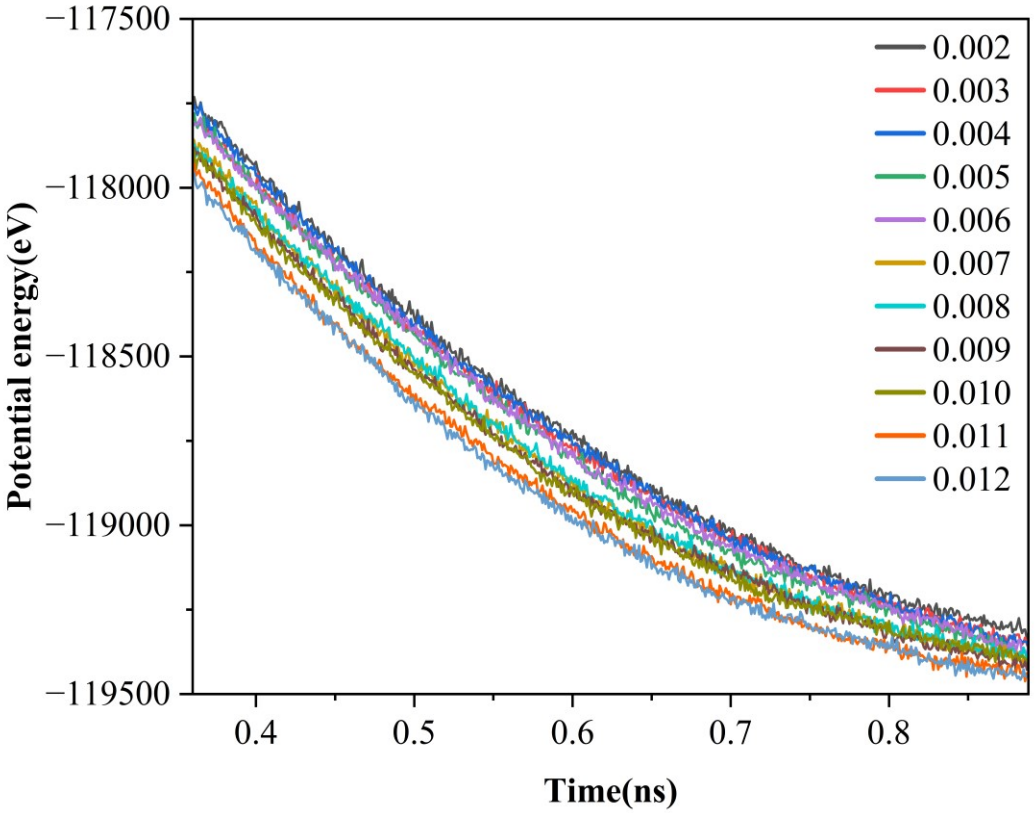


Fig. 10: Potential energy variation curve of water vapor condensation process on LC surface.

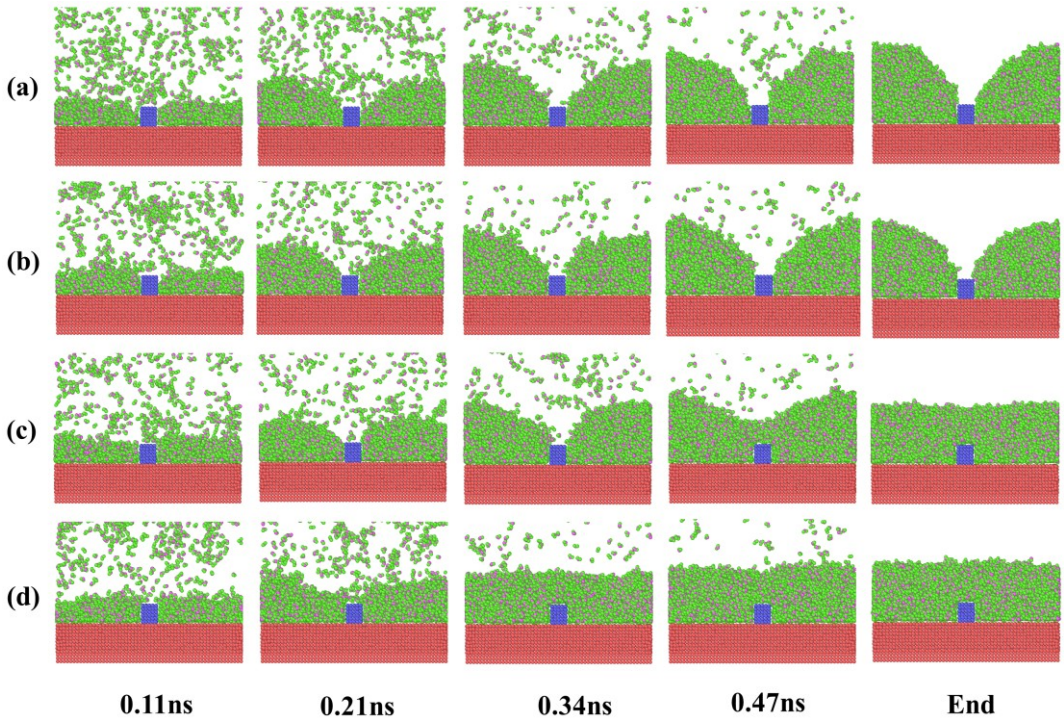


Fig. 11: Morphology of condensation process of water vapor on different wetting LC surfaces: (a) 0.002 eV; (b) 0.006 eV; (c) 0.007 eV; (d) 0.011 eV.

In Fig. 11(a) and (b), the condensation process maintains a dropwise mode throughout. In contrast, at a potential well depth of 0.007 eV, where the contact angle

undergoes an abrupt change, condensation initially proceeds in a dropwise manner. Subsequently, owing to the enhanced wettability of the nanoscale ribs, water molecules condensing on both sides find it easier to traverse the central rib, leading to coalescence of the condensation clusters from both sides. During the subsequent condensation stage, this coalescence diminishes the influence of the nanoscale ribs on the condensation morphology, allowing the process to proceed in a filmwise manner. In Fig. 11(d), at early condensation stages, the influence of the nanoscale ribs on the morphology is minimal. As the amount of condensed water increases, the clusters on both sides of the ribs merge and the subsequent condensation proceeds in a filmwise mode. This is consistent with the potential energy trends observed in Fig. 10: for potential well depths from 0.002 eV to 0.006 eV, the entire condensation process proceeds in the dropwise mode. For depths from 0.007 eV to 0.010 eV, the process initially involves dropwise condensation, but in the later stages, coalescence of condensation clusters triggers a transition to filmwise condensation. When the potential well depth exceeds 0.010 eV, the influence of the nanoscale ribs on the condensation morphology becomes negligible. We therefore posit that, at a potential well depth of 0.010 eV, the entire condensation process on the LC surface proceeds in a filmwise manner.

This general pattern is also observed in the MC and HC substrate groups. With increasing potential well depth, a pronounced decrease in the potential energy curve is evident. Similar to the LC group, the potential energy curves for the MC group exhibit significant overlap in the 0.002–0.004 eV range. However, beyond this range, the curves gradually decrease in height without exhibiting a sharp drop. In the HC group, a sudden drop in the potential energy curve occurs at a potential well depth of 0.008 eV. However, for depths below 0.008 eV, the curves do not exhibit significant overlap—an unusual behavior compared with the LC group that warrants further examination.

To elucidate this behavior, the condensation morphologies at various potential well depths for the MC group were analyzed, as shown in Fig. 13. In Fig. 13(a), the condensation process maintains a dropwise mode, and the final condensed water contacts the nanoscale ribs at a point below their top surface. At a potential well depth of 0.005 eV (Fig. 13(b)), the contact point of the final condensed water aligns with the top of the nanoscale ribs. However, unlike the LC surface, the initial condensation does not proceed in a dropwise mode. Owing to the combined effects of rib height and hydrophobicity, the condensed water is confined to the 两侧 of the nanoscale ribs, resulting in a final morphology that resembles water columns; however, at this stage, the condensation mode cannot be strictly classified as dropwise. Consequently, at 0.005 eV, the potential energy curves deviate from the 0.002–0.004 eV range. The combined influence of nanorib height and wettability gives rise to the phenomenon that even when the potential well depth is increased and the wettability becomes hydrophilic on the MC substrate, the final morphology can still retain a columnar state with a relatively large contact angle. Only when the potential well depth reaches 0.011 eV does the strong water–nanoscale rib interaction enable the condensation clusters on both sides to span across the nanocolumn, ultimately yielding a filmwise

final morphology. Based on previous studies [37–40], we consider that a hydrophilic state is achieved when the potential well depth exceeds 0.008 eV. It can thus be concluded that increasing the height of the nanoscale ribs effectively delays the transition from dropwise to filmwise condensation.

Fig. 14 illustrates the condensation process of water vapor on the HC substrate surface. In Fig. 14(a), the condensation process proceeds in a dropwise mode throughout. With increasing potential well depth (Fig. 14(b)), the initial condensation occurs in a dropwise mode. Over time, the contact point of the final condensed water aligns with the top of the nanoscale ribs. As shown in Fig. 9, the contact angle decreases progressively with increasing potential well depth, and at 0.008 eV, the final condensation morphology transitions to a filmwise state, accompanied by a significant drop in the potential energy curve. Prior to this threshold, a clear dropwise mode is observed during the initial condensation stage on the HC surface, consistent with the trend observed for the LC group. Thus, the height of the potential energy curve reflects differences in condensation modes, and variations in surface structure and wettability exert a significant influence on the condensation patterns.

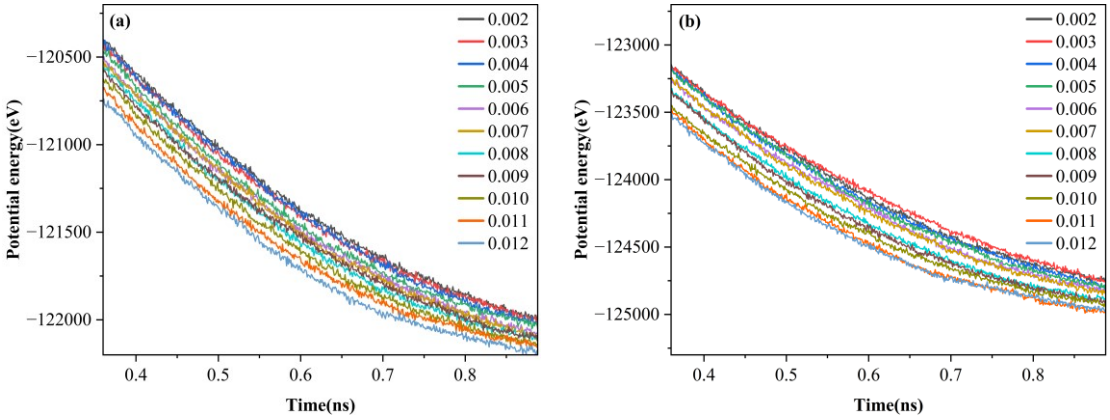


Fig. 12: Potential energy variation curve of water vapor condensation process on MC and HC surface: (a) MC surface; (b) HC surface.

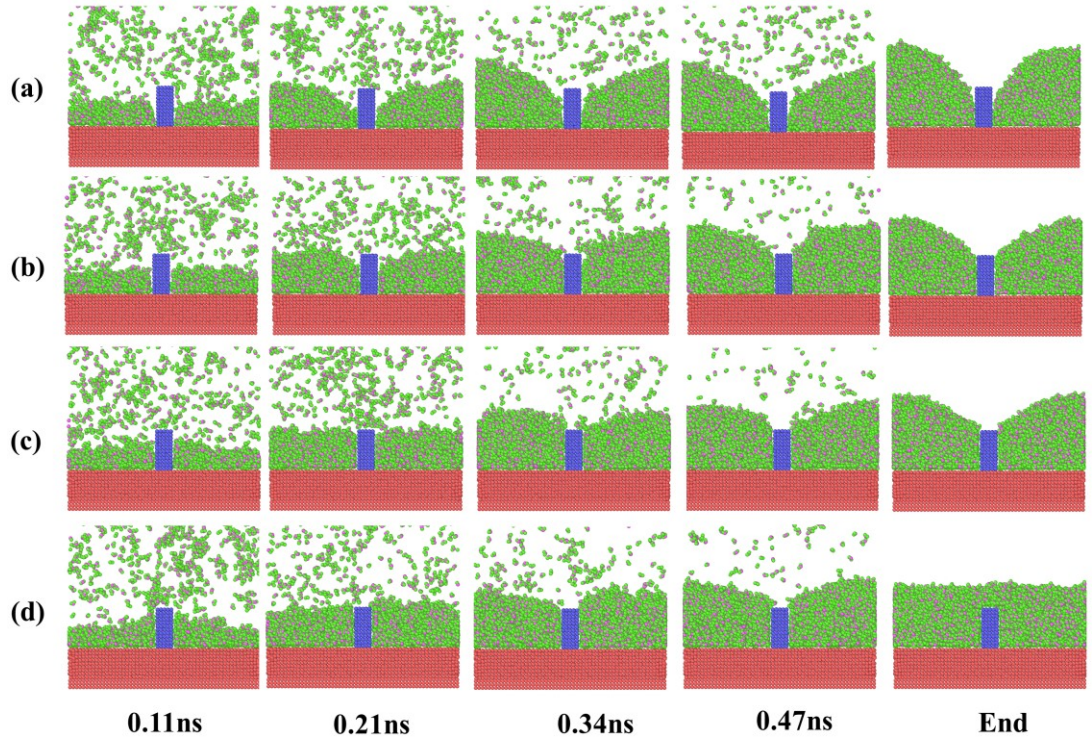


Fig.13: Morphology of condensation process of water vapor on different wetting MC surfaces: (a) 0.002 eV; (b) 0.005 eV; (c) 0.008 eV; (d) 0.011 eV.

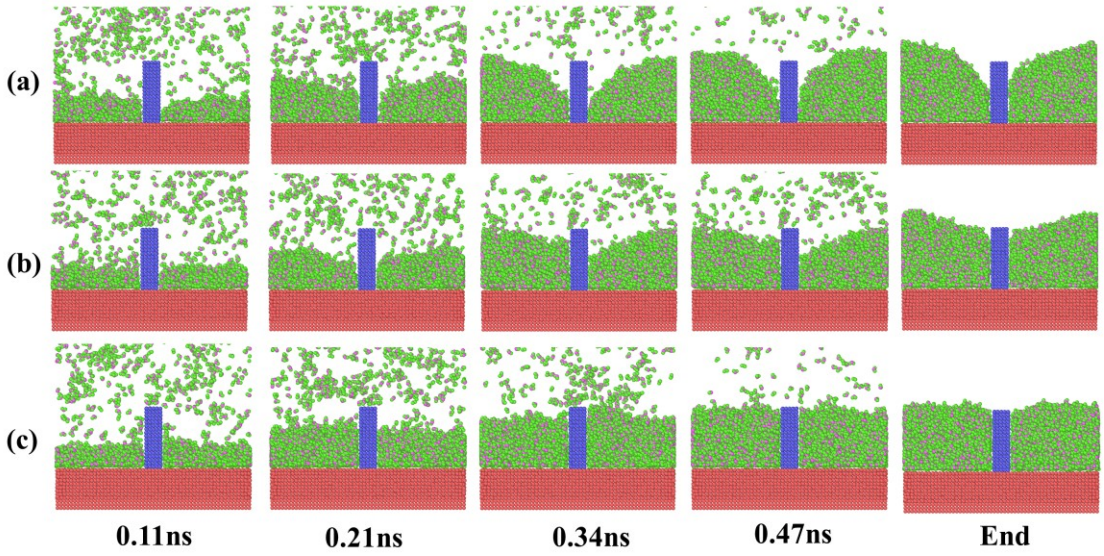


Fig.14: Morphology of condensation process of water vapor on different wetting HC surfaces: (a) 0.002 eV; (b) 0.005 eV; (c) 0.008 eV.

4. Conclusions

This study employs molecular dynamics simulations to investigate the transient condensation of water vapor on nanoribbed substrate surfaces. The simulation results demonstrate that both the height and wettability of the nanoscale ribs significantly influence the final condensation morphology of water vapor. Through systematic measurement of the contact angle and analysis of the transient condensation morphology, we found that on the LC substrate, the condensation mode is dropwise

for potential well depths of 0.002–0.006 eV. For depths of 0.007–0.010 eV, the process initiates in a dropwise mode but subsequently transitions to filmwise condensation. Beyond 0.010 eV, the condensation mode is entirely filmwise.

By appropriately increasing the nanorib height, the influence of wettability on the condensation morphology can be mitigated. On the MC substrate, even when the wettability reaches a hydrophilic level ($\varepsilon > 0.008$ eV), the final contact angle still exceeds 90°, and the morphology transitions to a filmwise state only when the potential well depth reaches 0.011 eV. When the characteristic height of the nanoscale ribs is comparable to the thickness of the condensed water layer, the wettability exerts a pronounced modulating effect on the condensation morphology, and the contact angle decreases rapidly with increasing wettability.

The gradient-height hydrophobic nanoscale rib configuration proposed in this study can serve as a reference for the surface modification design of atmospheric water-harvesting devices and low-temperature heat exchangers. By appropriately matching the nanoscale rib height with surface wettability, it is possible to elevate the critical potential well for the droplet-to-film condensation transition, sustain stable dropwise condensation over extended periods, and simultaneously enhance water collection efficiency and heat transfer performance.

Future research could be extended in three directions: (1) constructing hydrophilic–hydrophobic composite nanoscale rib structures to regulate droplet detachment behavior and investigate the effect of rib spacing; (2) incorporating airflow and temperature gradient fields to perform simulations that more realistically replicate atmospheric conditions; and (3) fabricating gradient nanoscale rib substrates and conducting macroscopic condensation experiments to validate the simulation findings presented in this study.

Declaration of Competing Interest

The authors declare that they have no known competing financial interests or personal relationships that could have appeared to influence the work reported in this paper.

CRediT authorship contribution statement

Chen Le: Investigation, Validation, Formal analysis, Writing - original draft. **Luo Zelong:** Investigation, Validation.**Ma Lianxiang:** Project administration, Funding acquisition. **Tang Yuanzheng:** Methodology, Writing - review & editing, Supervision.

Acknowledgment

This work was supported by the Natural Science Foundation of China (No. 52176077).

Reference

[1] Khawaji A D, Kutubkhanah I K and Wie J M 2008 Desalination 221 47
[2] Baco S, Abbas Q, Hayward T and Morley T 2021 J. Alloys Compd 881 160549
[3] Bhushan B 2020 Philos. Trans. R. Soc. A 378 20190440
[4] Humphrey J H, Brown J, Cumming O, Evans B, Howard G, Kulabako R N, Lamontagne J, Pickering A J and Wang E N 2020 Lancet Planet. Health 4 e91
[5] Jiao M, Yao Y, Chen C, Jiang B, Pastel G, Lin Z, Wu Q, Cui M, He S and Hu L 2020 ACS Mater. Lett 2 430
[6] Zhou X, Zhao F and Zhang P 2021 ACS Mater. Lett 3 1112
[7] Liu M, Wang S and Jiang L 2017 Nat. Rev. Mater 2 0007
[8] Tang Y, Yang X and Li Y 2021 Nano Lett 21 9824
[9] Zhu H, Cai S, Liao G, Gao Z F, Min X and Huang Y 2021 ACS Catal 11 14751
[10] Parker A R and Lawrence C R 2001 Nature 414 33
[11] Zheng Y, Han D, Zhai J and Jiang L 2008 Appl. Phys. Lett 92 084102
[12] Yu Z, Yun F F, Wang Y, Yao L, Dou S, Liu K, Jiang L and Wang X 2017 Small 13 1701403
[13] Wan Y, Zhang C and Zhang M 2021 Mater. Res. Express 8 055002
[14] Sharma V, Orejon D, Takata Y and Krishnan V 2018 ACS Sustain. Chem. Eng 6 6981
[15] Jin Y, Albaity M, Shi Y and Ghaffour N 2019 Int. J. Heat Mass Transf 144 118627
[16] Gao Y, Wang J and Xia W 2018 ACS Sustain. Chem. Eng 6 7216
[17] Gong L Y, Wei X D, Han T, Guo Y L and Shen S Q 2025 Acta Phys. Sin 74 143101 (in Chinese)
[18] Xing H W, Chen Z X, Yang L, Su Y, Li Y H and Hu H C 2024 Acta Phys. Sin 73 094701 (in Chinese)
[19] Nurrohman N, Almisbahi H, Tocci E, Abulkhair H, Albeirutty M, Othman R and Bamaga O 2024 Nanomaterials 14 1137
[20] Teodori M, Abbondanza D and Gallo M 2025 Phys. Rev. Res 7 043310
[21] Kim B M et al. 2025 Sci. Adv 11 adu8349
[22] Mehereen T, Chanda S, Nitu A A, Jami J T and Rahim R R 2024 arXiv:2411.10820 [cond-mat.mtrl-sci]
[23] Yang G, Zheng T, Cheng Q and Zhang H C 2024 Chinese Phys. B 33 044701
[24] Liu L X, Jiang M X, Gao N, Chen Y C, Hu W Y and Deng H Q 2025 Chinese Phys. B 34 046101
[25] Wang C, Peng P and Lai W S 2025 Chinese Phys. B 34 018101
[26] Shi Z, Zhong S and Zhang B 2024 Int. J. Heat Mass Transf 228 125623
[27] Wei L, Wang P and Chen X 2024 Surf. Interfaces 52 104981
[28] Wang Z J, Wang S Y and Wang D Q 2023 Int. J. Heat Mass Transf 205 123929
[29] Foiles S, Baskes M and Daw M S 1986 Phys. Rev. B 33 7983
[30] Mark P and Nilsson L 2001 J. Phys. Chem. A 105 9954
[31] Song F and Li B 2013 Langmuir 29 4266
[32] Rafiee J, Mi X and Gullapalli H 2012 Nat. Mater 11 217

[33] Andersen H C 1983 J. Comput. Phys 52 24
[34] Plimpton S 1995 J. Comput. Phys 117 1
[35] Stukowski A 2009 Modell. Simul. Mater. Sci. Eng 18 015012
[36] Cho H J, Preston D and Zhu Y 2016 Nat. Rev. Mater 2 0017
[37] Hu H, Li Q and Liu S 2019 Appl. Surf. Sci 494 249
[38] Niu D and Tang G 2014 Int. J. Heat Mass Transf 79 647
[39] Sheng Q and Sun J 2016 Sci. Rep 6 30764
[40] Niu D and Tang G 2016 Sci. Rep 6 19192